Control of structure topology and spatial distribution of biomacromolecules in protein@ZIF-8 biocomposites

Weibin Liang[†], Raffaele Ricco[‡], Natasha K. Maddigan[†], Robert P. Dickinson[†], Huoshu Xu[§], Qiaowei Li[§], Christopher J. Sumby[†], Stephen G. Bell[†], Paolo Falcaro*[‡], Christian J. Doonan*[†]

[†]Department of Chemistry and the Centre for Advanced Nanomaterials, The University of Adelaide, Adelaide, South Australia 5005, Australia

[‡]Institute of Physical and Theoretical Chemistry, Graz University of Technology, Stremayrgasse 9, Graz 8010, Austria

[§]Department of Chemistry, iChEM (Collaborative Innovation Center of Chemistry for Energy Materials), and Shanghai Key Laboratory of Molecular Catalysis and Innovative Materials, Fudan University, Shanghai 200433, P.R. China

KEYWORDS: biomimetic mineralization, metal-organic frameworks, confocal laser scanning microscopy

ABSTRACT: The protective capacity and applications of biomimetically mineralized biomacromolecule zeolitic imidazolate framework (ZIF) composites is likely dependent on the localization of the biomolecule and the topology of the mineralized ZIF coating. Herein we identify reaction conditions to reliably yield the porous ZIF-8 sodalite topology (high ZIF-8 precursor concentrations; high 2-methylimidazole:Zn^{2+} ratios) in preference to other more dense phases and protocols to universally prepare such biocomposites with a range of biomacromolecules. Through the use of fluorophore tagged proteins and confocal laser scanning microscopy (CLSM) we further establish the positioning of biomolecules within ZIF-8 crystals. CLSM reveals subsurface localization with fluorescein-tagged bovine serum albumin (BSA) or full encapsulation with rhodamine B-tagged BSA. These observations allowed us to demonstrate that core-shell ZIF-8 growth strategies afford complete encapsulation, with varying thicknesses of potentially active biocomposite or protective ZIF-8. The demonstrated control over ZIF topology (enabling mass transport) and biomacromolecule localisation is critical for applications of MOF biocomposites in catalysis.

INTRODUCTION

Metal-organic frameworks (MOFs) are a class of materials well-known for their high degree of crystallinity and ultra-high porosity.[1-3] A salient feature of MOF chemistry is that their modular synthesis from organic links and metal nodes allows for precise control of structure topology, pore size and chemical functionality.[4] Recently, MOFs have been explored for their potential to form novel biocomposites with proteins,[5-7] viruses[8] and living cells[9],[10] by a process termed biomimetic mineralization.[11] To date, the most widely studied MOF for this application is zeolitic imidazolate framework-8[12, 13] (ZIF-8 or ***sod***-$Zn(mIM)_2$, ***sod*** = sodalite, mIM = 2-methylimidazole).[11, 14-16] ***Sod***-$Zn(mIM)_2$ is a robust, three dimensional network, composed of tetrahedral Zn^{2+} nodes linked together *via* mIM ligands,[17, 18] which can be synthesized in aqueous conditions at room temperature.[19] Typically, Zn^{2+} and mIM are combined with the target biomacromolecules (or cells) in aqueous solution at room temperature and the MOF-based biocomposite is formed within minutes.[5, 6] Characterization of the MOF biocomposites formed from proteins or enzymes indicates that the biomacromolecules are encapsulated within the ZIF-8 crystals.[11] The ***sod***-$Zn(mIM)_2$ coating was shown to protect the biomacromolecules from conditions that would normally lead to their denaturation.[5, 6, 11] For example, when encapsulated within ***sod***-$Zn(mIM)_2$ crystallites the enzyme horseradish peroxidase (HRP) retained activity after immersion in boiling water or *N,N'*-dimethylformamide (DMF, b.p. 153 °C).[6] Accordingly, these novel MOF biocomposites show great promise for application to industrial biocatalysis where strategies for enhancing enzyme stability are of significant interest.[11, 20, 21]

An important aspect of this chemistry that has not been addressed is the effect of reaction conditions on the topology of the ZIF coating.[22-24] ZIF-8 was identified to have a sodalite topology with pore apertures and diameters of *ca.* 3.4 Å and 11.4 Å, respectively, and a BET surface area of 1531 $m^2\ g^{-1}$.[12, 13] However, experimental and theoretical studies have shown that the ***sod*** structure is one of many energetically accessible polymorphs for networks constructed from Zn^{2+} and mIM building units.[23-26] Indeed, in neat H_2O a variety of different structures can be synthesized by simply modifying the precursor concentration and/or molar ratio between Zn^{2+} and mIM.[22, 27, 28] Similarly, we have found that minor changes to the standard experimental conditions,[6] such as the ratio of the ZIF precursor concentrations, also leads to a variety of different network topologies. Thus, to reliably afford specific ZIF structures

a fundamental understanding of the reaction conditions is required. This data is critical to the development of these MOF biocomposites for catalytic applications, as the framework topology can have a marked effect on the performance characteristics of the catalyst.[29] For example, ***sod***-Zn(mIM)$_2$ behaves as a microporous materials towards N_2 isothermal adsorption, while the more thermodynamically stable polymorph, ***dia***-Zn(mIM)$_2$ (***dia*** = diamond) does not (i.e. it is non-porous) due to its more densely packed structure.[22] As a result, these two ZIF coatings would confer distinct size selectivity and mass diffusion properties to biocomposites.[30] Also, the spatial distribution of the biomacromolecules within the crystals will influence the catalytic efficacy of the MOF biocomposites.[27] Comparable studies have shown that the distribution of inorganic nanoparticles within ZIF-8 crystals is dependent on synthetic conditions.[31]

Here we want to verify if the distribution of biomacromolecules throughout the ***sod***-Zn(mIM)$_2$ crystallite can be controlled by modifying the synthesis conditions. We carried out a systematic study to ascertain the specific synthesis conditions required to achieve pure ***sod***-Zn(mIM)$_2$ biocomposites and present a facile and general method for the precise control of the particle size of the biocomposites. Furthermore, we studied the spatial distribution of the biomacromolecules within the ZIF crystals by encapsulating fluorophore-tagged bovine serum albumin (fluorescein-tagged BSA (FBSA) and rhodamine B-tagged BSA (RbBSA)) and examining them *via* confocal laser scanning microscopy (CLSM). The exploration of MOF-based biocomposites where biomacromolecules are encapsulated within the crystals is of high interest[5, 6, 9, 10, 14-16, 31] and this study provides a blueprint for how to tailor the physical properties of the composites and provides insight into the underlying growth mechanism of these systems.

EXPERIMENTAL SECTION

Syntheses

All chemicals, biomolecules (alcohol oxidase, solution from *Pichia pastoris*, buffered aqueous solution, 10-40 units/mg protein (biuret), Sigma-Aldrich; bovine serum albumin, ≥96%, lyophilized powder (agarose gel electrophoresis), Sigma-Aldrich; peroxidase from horseradish, lyophilized powder, beige, ~150 U/mg, Sigma-Aldrich; Urease, from *Canavalia ensiformis* (Jack bean), Type III, powder, 15,000-50000 units/g solid, Sigma-Aldrich; hemeoglobin human, lyophilized powder, Sigma-Aldrich; myoglobin, from equine skeletal muscle, 95-100%, essential salt-free, lyophilized powder, Sigma-Aldrich; catalase, from bovine liver, lyophilized powder, 2,000-5,000 units/mg protein, Sigma-Aldrich; lysozyme, egg white, >20,000 U/mg, Astra Scientific; trypsin, BRP, European Pharmacopoeia (EP) reference standard, Sigma-Aldrich) and solvents were purchased from commercial sources and used as received without further purification.

Fluorophore-tagged biomolecules

0.5 mg of fluorescein isothiocyanate (FITC), or rhodamine B isothiocyanate (RbITC), and 40 mg of biomacromolecule (bovine serum albumin (BSA), horseradish peroxidase (HRP), trypsin (TR), hemoglobin (HGB), alcohol oxidase (AOx), urease, or myoglobin (MB)) were dissolved in 4 mL of carbonate-bicarbonate aqueous buffer solution (0.1 M, pH 9.2) and left for twelve hours in darkness at 4°C under gentle stirring. The fluorophore-tagged biomacromolecule (fluorescein-tagged biomacromolecules (F-BSA, F-AOx, F-HRP, F-HGB, F-MB and F-TR, F-urease) and rhodamine B-tagged biomacromolecules (Rb-BSA, Rb-AOx, Rb-HRP, Rb-HGB, Rb-MB and Rb-TR, Rb-urease)) was recovered by passing the reaction mixture through an Illustra NAP-25 column (GE Healthcare Life Sciences, NSW, Australia). Then the crude protein/enzyme solution was concentrated through a 10 kDa membrane by centrifugation at 4 °C (4,000 rpm for 20 min), followed by solvent-exchange with ultrapure water. The concentration/solvent-exchange process was repeated two times to ensure the complete removal of buffer salts in the solution. Thereafter, the concentrated fluorophore-tagged protein/enzyme solution was passed through an NAP-25 column again to ensure the completely removal of unreacted FITC or RbITC molecules. The obtained fluorophore-tagged protein/enzyme solution was stored in darkness at 4 °C.

Synthesis parameter screening for the ZIF polymorphs

In a typical experiment for ZIF polymorph synthesis, the desired volume of 0.24 M *aq.* $Zn(OAc)_2{\cdot}2H_2O$ and 3.84 M *aq.* 2-methylimidazole (HmIM) were mixed in water. $Zn(OAc)_2{\cdot}2H_2O$ concentration (80 mM, 40 mM, 20 mM, and 10 mM) and HmIM/Zn molar ratio (HmIM/Zn^{2+} = 16, 8, 4, 2, and 1) were adjusted to study their effect on ZIF polymorph formation. The reaction mixture was left under static or stirred conditions at room temperature for 24 h. After synthesis, the precipitates were collected by centrifugation (10,000 rpm for 5 min) and measured by PXRD without washing. The PXRD patterns were compared to the simulated data to identify the ZIF phases in samples. Results were then summarized as ternary plots of [$Zn(OAc)_2$] vs [HmIm] vs [H_2O].

Synthesis parameter screening for biomimetic mineralized growth of *sod*-Zn(mIM)$_2$

The procedure for screening the synthesis parameters for the biomimetically mineralized growth of ***sod***-Zn(mIM)$_2$ was analogous to abovementioned screening experiments for the ZIF polymorphs with the exception that 1 mg of biomacromolecule was added in the reaction mixture. Nine types of biomacromolecules were chosen for the screening experiments: BSA, FBSA, HRP, catalase, TR, HGB, AOx, lysozyme, and MB.

Synthesis method for FBSA-@-*sod*-Zn(mIM)$_2$

FBSA-@-***sod***-Zn(mIM)$_2$ was synthesized in water with 40 mM of $Zn(OAc)_2{\cdot}2H_2O$, 640 mM of HmIM and 0.33 mg mL^{-1} FBSA at room temperature under static condition for 24 h. The precipitate was recovered by centrifugation at 10,000 rpm for 5 min and then washed, sonicated, and centrifuged twice each in pH 7.5 TBS buffer (1.5 mL, TBS = tris-buffered saline, 50 mM Tris-Cl and 150 mM NaCl) followed by ethanol (1.5 mL). Thereafter, the sample was

immersed in 10% w/w sodium dodecyl sulfate (SDS) solution for 30 min (1.5 mL, in pH 7.5 TBS buffer) to remove surface adsorbed FBSA. This was followed by pH 7.5 TBS buffer (1.5 mL, 2x) and ethanol (1.5 mL, 2x) washes to remove residual surfactant.

Characterization

Powder X-ray diffraction (PXRD)

PXRD patterns were obtained using a D4 ENDEAVOR X-ray Diffractometer from Bruker. A Co anode was used to produce K_α radiation (λ = 1.78897 Å). Flat plate diffraction data was collected from the range 2θ = 5-40 °. The PXRD data were expressed as the copper-source irradiated patterns (λ = 1.54056 Å) using PowDLL Converter (version 2.68.0.0).

Thermogravimetric analysis (TGA)

TGA data was collected on a Simultaneous Thermal Analysis–STA (TGA/DSC) from LINSEIS THERMAL ANALYSIS. Approximately 5 mg of sample was placed on a ceramic pan and heated from 30 to 800 °C at a rate of 5 °C min^{-1}. Each sample was heated under a constant flow of *ca.* 30 L min^{-1} air.

Fourier transform infrared (FTIR) spectroscopy

FTIR spectra of ZIFs and biomacromolecule/ZIF composites were obtained on a Perkin Elmer Spectrum 100 FT-IR Spectrometer using approximately 0.5 mg of sample. Sixteen scans were recorded over the range of 650-4000 cm^{-1}.

Gas sorption

Gas adsorption isotherms were obtained on a Micromeritics 3Flex Surface Characterisation Analyser. Approximately 20 mg of sample was placed into a glass analysis tube and degassed under dynamic vacuum for 12 h at 105 °C prior to measurement.

Nitrogen (N_2) adsorption and desorption isotherms were measured at 77 K. The isotherms were then analyzed to determine the Brunauer-Emmet-Teller (BET) surface area using the MicroActive software (Version 3.00, Micromeritics Instrument Corp. 2013).

Confocal laser scanning microscopy (CLSM)

The presence and spatial location of the fluorophore-tagged biomolecules in (or on) the MOFs composites was determined using CLSM technique (Olympus FV3000 Confocal Laser Scanning Microscope, OLYMPUS). The fluorescein-tagged biomolecules were excited at 488 nm and the fluorescence signal was collected in a window from 495 to 545 nm. The rhodamine B-tagged biomolecules were excited at 561 nm and the fluorescence signal was collected in a window from 570 to 620 nm.

Fluorescence spectrophotometry

Fluorescence measurements of solution samples were carried out using a Varian Cary Eclipse Fluorescence Spectrophotometer.

Scanning Electron Microscopy (SEM)

SEM images were collected using a Philips XL30 Field Emission Scanning Electron Microscope (FESEM). Prior to analysis, the samples were dispersed in ethanol by sonication, drop-cast on a 12 mm aluminum SEM stage, and sputter-coated with a 5 nm platinum thin film.

Zeta potential measurements

Zeta potential information was obtained on a Malvern ZetaSizer dynamic light scattering instrument.

RESULTS AND DISCUSSION

ZIFs are composed of tetrahedral metal centers connected *via* imidazole links.[32] This node structure gives rise to networks that resemble silica polymorphs.[32, 33] A salient difference between these materials is that the structures of ZIFs are largely determined by the chemistry of the bridging imidazole units.[25, 33] Nevertheless, for mIM and Zn^{2+} a number of different polymorphs have been experimentally observed such as ***dia*** and katsenite.[22-24, 28] Based on the packing density and orientation of the organic ligands, these topologies can have vastly different physical properties.[22-24] In our examination of the biomimetic mineralization of different proteins we found that a stoichiometric HmIM/Zn ratio of 4:1 afforded a variety of structural topologies in addition to ***sod*** (Figure S1 -S2).[27, 28] Further, we found that the preparation conditions (*i.e.* stirred *versus* non-stirred solutions) affected the reaction rate of ZIF formation. Thus, we were motivated to understand the influence of reaction conditions on these systems and to uncover a general method to synthesize biocomposites of predetermined topology. To achieve this aim we carried out systematic screening experiments to ascertain the effect of the HmIM/Zn ratio on the structure of the biocomposite. We varied the zinc acetate concentration in the reaction mixture (80, 40, 20, and 10 mM), HmIM/Zn molar ratio (HmIM/Zn = 16, 8, 4, 2, and 1), mechanical agitation (stirred and non-stirred solutions), and biomacromolecule (BSA, FBSA, HRP, catalase, TR, HGB, AOx, lysozyme, and MB) (Figure 1b, S1, and S2). The typical synthesis procedure was carried out as follows: an aqueous solution of HmIM was mixed with an aqueous solution of the biomacromolecule (or water for control experiments), followed by the addition of an aqueous solution of zinc acetate. It is worth noting that this addition sequence of reactants was chosen because: 1) the alkaline HmIM aqueous solution facilitated protein dissolution; 2) the formation of precipitates is prevented (in the absence of HmIM ligand, zinc acetate mixed with proteins can induce the formation of precipitates). After preparation, the mixture was left at room temperature for 24 h, subsequently the ZIF biocomposites (or pure ZIFs) were recovered by centrifugation. The precipitates were examined by PXRD without further treatment and the resulting PXRD patterns were compared to the simulated data to identify the ZIF phases present. A summary of the results is presented (Figures 1b, S1-S3) as ternary plots.

In the absence of biomacromolecules, the PXRD results show that a high precursor concentration ($Zn(OAc)_2$ and HmIM) and/or a high HmIM/Zn molar ratio favor the formation of ***sod***-$Zn(mIM)_2$, (Figure S1- S2). However, at dilute and/or low HmIM/Zn molar ratio ***dia***-$Zn(mIM)_2$, an amorphous product (***amorph***-$Zn(mIM)_2$, ***amorph*** = amorphous) and new structures of unidentified topologies

(named U12, U13, and U14) were found to be the dominant products (Figure 1b, S1-S2). We noted that stirring during synthesis accelerated the product formation, however; the general trend of the phase diagrams (*vide infra*) remained unchanged (Figure 1b and S2). U14 was produced exclusively under mechanical agitation, however; U12 can be formed with or without stirring (Figure 1b, S2–S3). The three structures that could not be identified as known ZIF materials (U12, U13, and U14) were further investigated (Figure S1-S8). FTIR and TGA analysis performed on U13 are consistent with its assignment as a derivative of zinc hydroxide (Figure S5-S8). FTIR and TGA studies confirmed the presence of a HmIM ligand, with a HmIM/Zn molar ratio of 2 for U14 and 1 for U12 (Figure S5-S6).

According to the ternary plot, we synthesized ***sod***-Zn(mIM)$_2$, ***dia***-Zn(mIM)$_2$, U12, and U14 to further study the properties of these polymorphs. The phase purity of the bulk samples were confirmed by PXRD analysis (Figure S3-S4) and the particle morphology was assessed by SEM (Figure S7). Analysis of the SEM images showed that ***sod***-Zn(mIM)$_2$ afforded rhombic dodecahedron crystals of size distribution 85.7 ± 0.1 µm (Figure S7). However, for ***dia***-Zn(mIM)$_2$, U12, and U14 structures, elongated hexagonal plates, octahedral, and spindle-shape plate morphologies were observed, respectively (Figure S7). The permanent porosity of each material was assessed by 77K N_2 gas adsorption isotherms. Analysis of these data yielded Brunauer-Emmett-Teller surface area values of 1358.5, 22.9, 50.9, and 26.0 m^2 g^{-1} for ***sod***-Zn(mIM)$_2$, ***dia***-Zn(mIM)$_2$, U12, and U14, respectively (Figure S8). In summary, these data imply that ***dia***-Zn(mIM)$_2$, U12, and U14 are densely packed polymorphs which is consistent with the synthetic conditions used. For example, high HmIM concentrations are known to enhance the rate of reaction by increasing the pH of the reaction mixture[34], thus leading to the isolation of the lower density ***sod*** framework. Furthermore, dilute reactant concentrations are known to give rise to dense ZIFs[23] which are consistent with the physical properties of ***dia***-Zn(mIM)$_2$, U12, and U14.

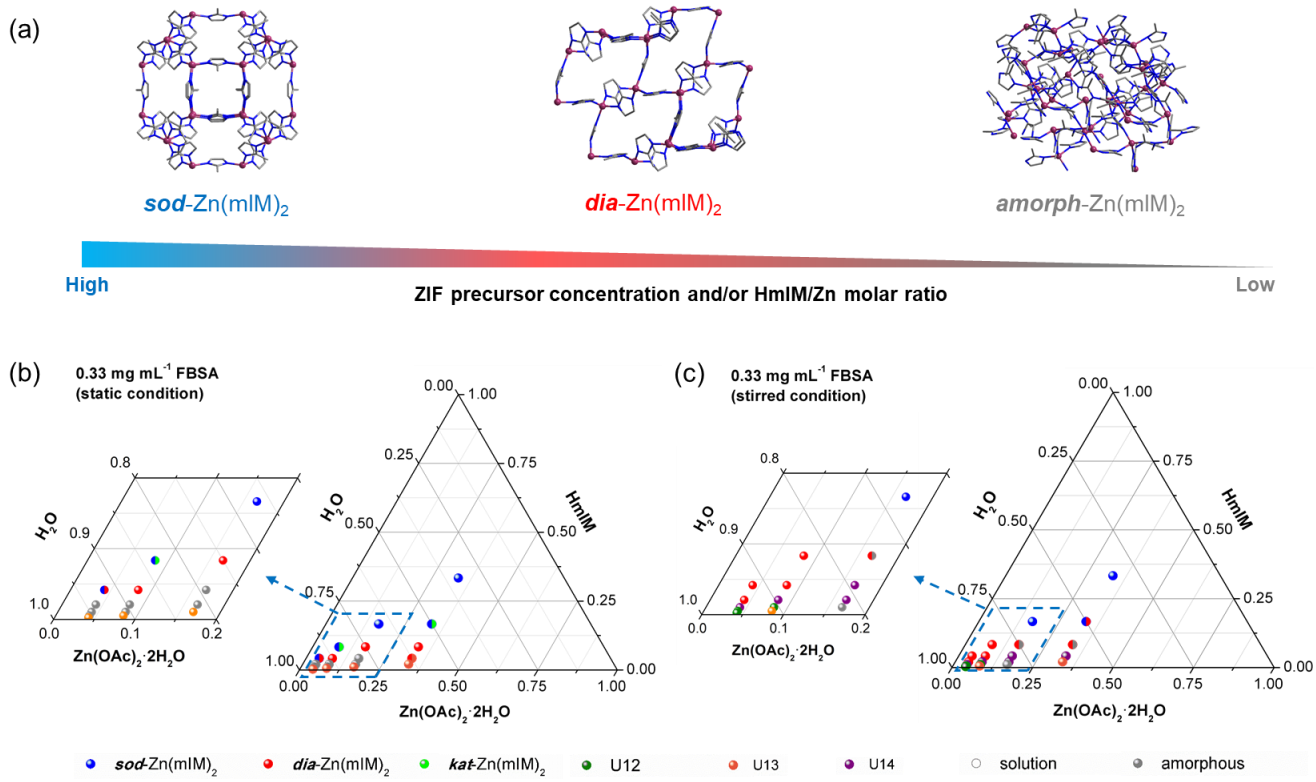

Figure 1. (a) Molecular representation of ***sod***-Zn(mIM)$_2$, ***dia***-Zn(mIM)$_2$, and ***amorph***-Zn(mIM)$_2$. (b) and (c) Ternary graphs (by volumetric fraction) of 0.33 mg mL^{-1} aqueous solution of fluorescein-tagged bovine serum albumin (FBSA,), 0.24 M aqueous solution of Zn(OAc)$_2$·2H$_2$O, and 3.84 M aqueous solution of 2-methylimidazole (HmIM) showing the ZIFs plots at different Zn(OAc)$_2$·2H$_2$O concentrations (80 mM, 40 mM, 20 mM, and 10 mM), molar-ratios between HmIM and Zn^{2+} (HmIM/Zn^{2+} = 16, 8, 4, 2, and 1) and mechanical agitation (static (b) and stirred condition (c)).

The phase screening protocol for the biomimetically mineralized growth of the ZIF-biocomposites were analogous to those performed in the absence of biomacromolecules (*vide supra)* with the exception that a solution of 1 mg of protein/enzyme (in place of water) was added to the reaction mixture (Figure 1b and S1-S3). The results of the PXRD analysis indicate that the introduction of biomacromolecules (BSA, FBSA, HRP, catalase, TR, HGB, AOx, lysozyme, and MB) does not affect the general trend of the product distribution observed in the ternary plot (Figure 1b and S1-S3): *i.e.* that increasing the HmIM/Zn ratio leads to the lower density topology ***sod***. However, it is

worth noting that the ***amorph***-Zn(mIM)$_2$can be transformed to ***sod***-Zn(mIM)$_2$ by ethanol washing (Figure S9-S12).

An important outcome of this work is that the ternary plots provide guidelines for the conditions required to synthesize ZIF biocomposites of predetermined topology. High HmIM/Zn ratios and high precursor concentration accelerate the ZIF formation and favor the crystallization of the kinetic polymorph, ***sod***-Zn(mIM)$_2$. This is consistent with reports that ZIF formation is accelerated by the addition of base to the reaction mixture as it results in a higher concentration of deprotonated HmIM ligands.[34] Furthermore, under dilute conditions and/or low HmIM/Zn ratios, the reaction kinetics are slower, and the more thermodynamically stable materials are the predominant products (***dia***-Zn(mIM)$_2$, ***amorph***-Zn(mIM)$_2$, U12, U13, and U14, Figure 1b, S1-S2, and S6).[11, 24] It is worth noting that the exotic ZIF phase, katsenite (***kat***), reported by T. Friščić and co-authors using a mechanical milling approach[23] has been identified in the present work as an impurity formed in aqueous conditions. Although the introduction of biomacromolecules enhances the ZIF formation kinetics,[6] the same ZIF topologies are identified as observed under protein-free conditions. This result is a strong evidence that the biomacromolecules do not direct the topology of the ZIF structure, but can induce their formation.

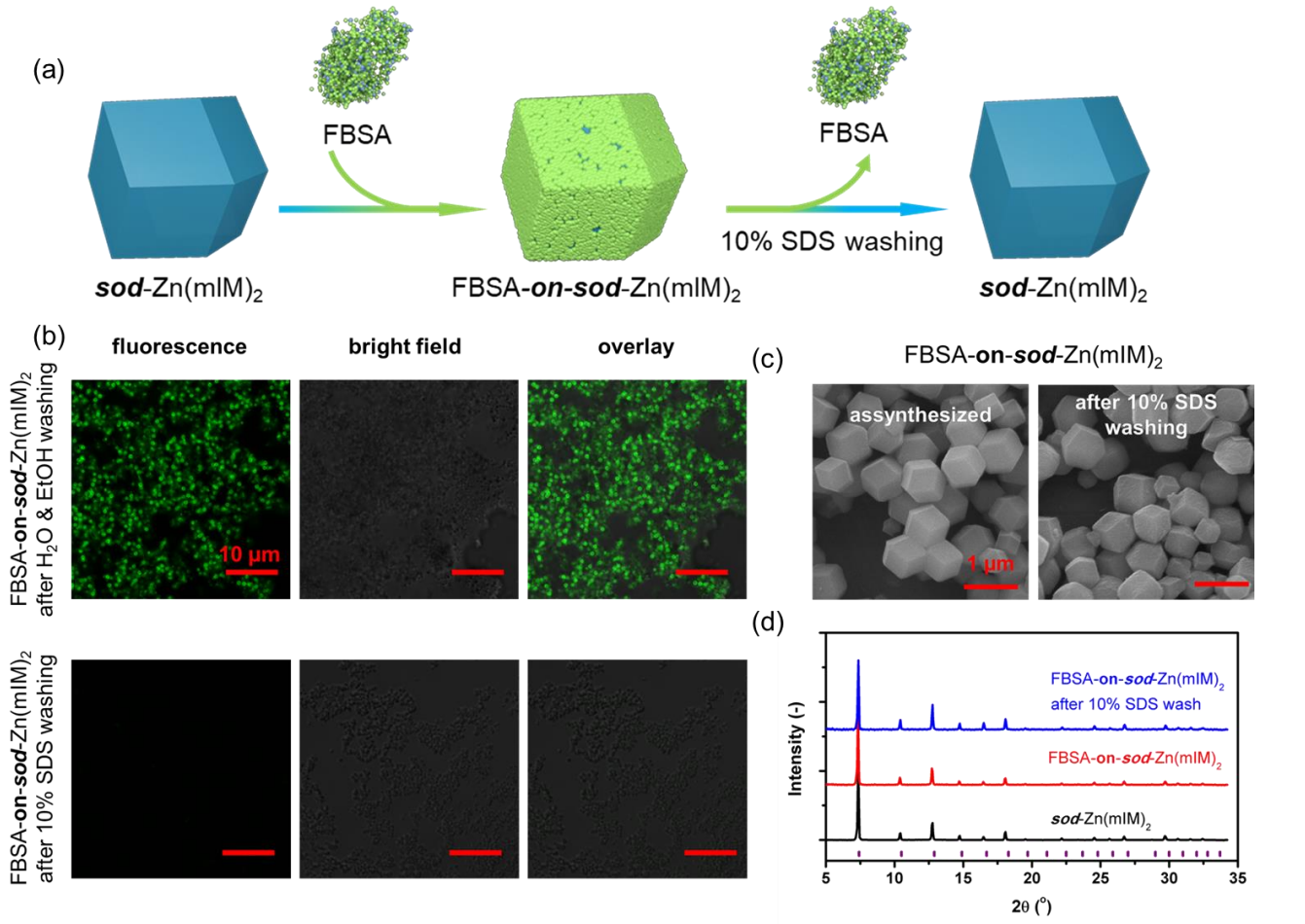

Figure 2. (a) Schematic diagram demonstrating the synthesis method for FBSA-**on**-***sod***-Zn(mIM)$_2$ and the removal of the surface-adsorbed FBSA on FBSA-**on**-***sod***-Zn(mIM)$_2$ by 10% SDS treatment (w/w, in pH 7.5 TBS buffer; SDS = sodium dodecyl sulfate). (b) Confocal laser scanning micrographs showing the fluorescence, bright field, and overlay images of FBSA-**on**-***sod***-Zn(mIM)$_2$ after H_2O and EtOH washing and FBSA-**on**-***sod***-Zn(mIM)$_2$ after 10% SDS washing. (c) SEM images of the as-synthesized FBSA-**on**-***sod***-Zn(mIM)$_2$ (left) and the sample after 10% SDS washing (right). (d) Experimental PXRD patterns of as-synthesized ***sod***-Zn(mIM)$_2$ (black), as-synthesized FBSA-**on**-***sod***-Zn(mIM)$_2$ (red), and FBSA-**on**-***sod***-Zn(mIM)$_2$ after 10% SDS treatment.

Among the different ZIF polymorphs, ***sod***-Zn(mIM)$_2$ has been exclusively studied. Presumably this because the open architectures and relatively large pore volumes of ***sod***-Zn(mIM)$_2$ have been shown to facilitate selective molecular transport from the external environment to the

encapsulated biomacromolecule.[6, 31] This property has allowed biocatalytic reactions to be assessed for ***sod***-Zn(mIM)$_2$-biocomposites.[11] Thus, due to the more densely packed, non-porous nature of ***dia***-Zn(mIM)$_2$ U12, and U14 (Figure S8) we targeted the ***sod***-Zn(mIM)$_2$-biocomposite for further analysis.

In addition to determining the conditions required to synthesize phase pure biocomposites, understanding the spatial distribution of the biomacromolecules within the ***sod***-Zn(mIM)$_2$ is essential to applications such as biocatalysis. Accordingly, BSA was labelled with fluorescein isothiocyanate (FITC) to afford fluorophore-tagged protein (FBSA), then confocal laser microscopy (CLSM) was employed to ascertain the location of FBSA within the ***sod***-Zn(mIM)$_2$-biocomposites. The resulting FBSA-@-***sod***-Zn(mIM)$_2$ biocomposite was used as a model system.

Proteins can be deposited on the outer surface of MOF crystals by means of electrostatic interactions, or covalent bonding.[11] Thus an important first step is the application of a washing protocol to remove the surface-adsorbed FBSA. This will prevent the observation of luminescent signals from non-encapsulated protein. To develop an effective washing protocol we first synthesized composites where FBSA is surface-bound, FBSA-**on**-***sod***-Zn(mIM)$_2$ (Figure 2a). Typically, FBSA-**on**-***sod***-Zn(mIM)$_2$ was synthesized by mixing FBSA with ***sod***-Zn(mIM)$_2$ crystals in water at room temperature for 1 hour (Figure 2a). The surface-adsorption of FBSA molecules on ***sod***-Zn(mIM)$_2$ could be detected by eye as the crystals were yellow in appearance. The material was then investigated using CLSM and the fluorescent images of the compound are shown in Figure 2b. The as-synthesized FBSA-**on**-***sod***-Zn(mIM)$_2$ were subsequently washed twice with water and ethanol, followed by 10% surfactant (Triton X100 (T100) or sodium dodecyl sulfate (SDS), w/w, in TBS buffer (pH 7.5)). The CLSM images clearly show that water/ethanol and 10% T100 washing are not sufficient to remove the surface-adsorbed FBSA on ***sod***-Zn(mIM)$_2$ (Figure 2b and S14). However, no fluorescence signal was observed for FBSA-**on**-***sod***-Zn(mIM)$_2$ after 10% SDS treatment, indicating complete removal of the absorbed FBSA molecules from the surface of ***sod***-Zn(mIM)$_2$ (Figure 2b). Importantly, PXRD and SEM analysis show that the crystallinity and particle morphology of ***sod***-Zn(mIM)$_2$ are essentially identical subsequent to the washing procedure (Figure 2c and d). Thus, the following washing protocol was applied to all samples to ensure the removal of surface bound protein: 1) wash twice with H_2O and ethanol to remove the unreacted precursors; 2) disperse and soak crystals in 10% SDS for 30 min at room temperature to remove the surface adsorbed biomacromolecules; 3) wash twice with TBS buffer and ethanol to remove the residual SDS. Therefore, the use of this protocol allows for selective removal of FBSA from the MOF crystals surface without compromising the integrity of the ***sod***-Zn(mIM)$_2$ particles.

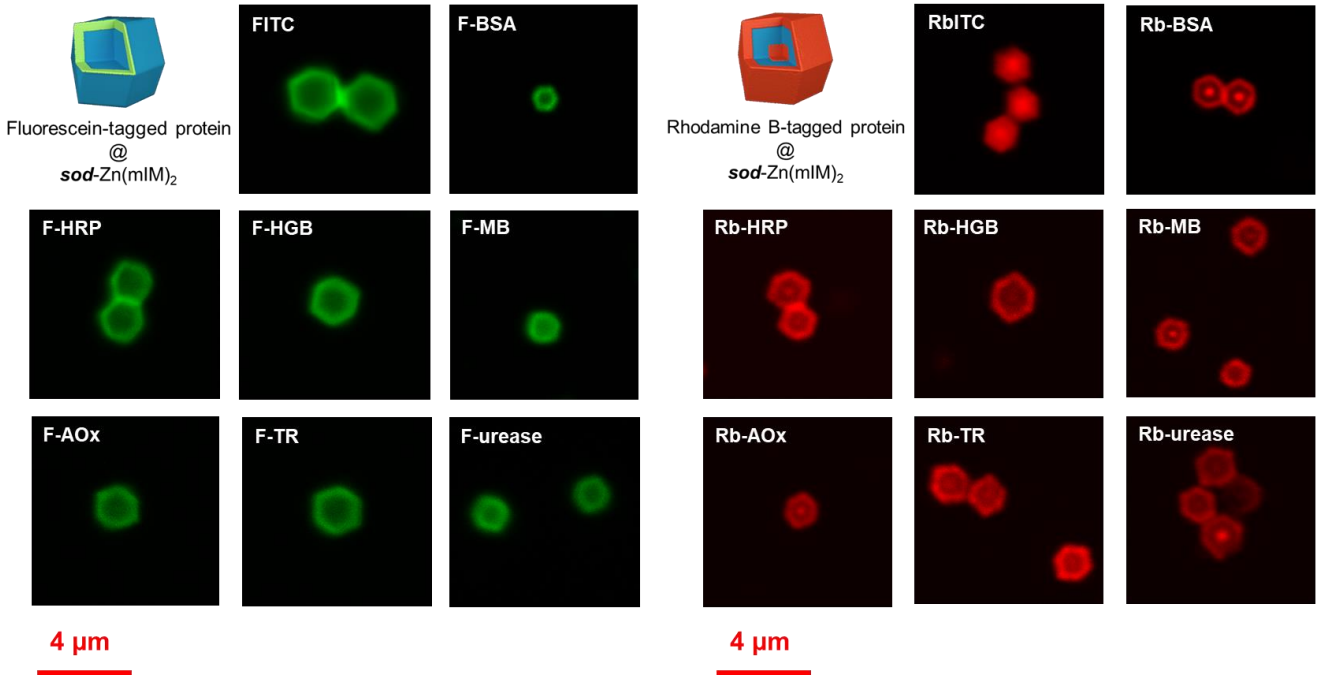

Figure 3. CLSM fluorescence images of ***sod***-Zn(mIM)$_2$ synthesized in the presence of FITC, RbITC, and fluorescein- (or rhodamine B-) tagged AOx (F-AOx or Rb-AOx), HRP (F-HRP or Rb-HRP), HGB (F-HGB or Rb-HGB), MB (F-MB or Rb-MB), trypsin (F-TR or Rb-TR), and urease (F-urease or.Rb-urease).

In a typical experiment for the biomimetically mineralized growth of FBSA/***sod***-Zn(mIM)$_2$, an aqueous solution of 40 mM $Zn(OAc)_2$, 640 mM HmIM and 0.33 mg mL^{-1} FBSA was prepared and allowed to stand at room temperature for 24 h. We note that static synthetic conditions gave rise to slightly larger crystallites than mechanically stirred reactions (SEM and CLSM images, 1.58 ± 0.15

versus 1.33 ± 0.14 µm, Figure S15-S20). In addition, for a fixed $Zn(OAc)_2$ concentration, smaller FBSA-@-***sod***-$Zn(mIM)_2$ particles can be synthesized by using a higher FBSA dosage and/or higher HmIM/Zn ratio in the reaction (Figure S15-S20).

We quantified the FBSA immobilization efficiency by dissolving the FBSA-@-***sod***-$Zn(mIM)_2$ biocomposite in 0.1 M citric-sodium citrate aqueous buffer (pH 5.0) and analyzed the FBSA fluorescence signal *via* spectroscopically (Table S1). The immobilization efficiency (average of five independent analyses) was calculated to be 74-89% before 10% SDS washing *versus* 32-42% after 10% SDS washing (Table S1). These data confirm that 40-45% of the FBSA is surface bound while 50-55% is encapsulated in the MOF crystal. We acknowledge that the extent of encapsulation efficiency is presumably biomacromolecule dependent, however, these experiments did address the importance of a post-synthetic surfactant washing procedure. Furthermore, CLSM analysis demonstrates that the FBSA molecules are predominantly encapsulated in the sub-surface region of the ***sod***-$Zn(mIM)_2$ crystallites rather than homogeneously distributed throughout the crystal (Figure 3).[6] These results suggest that under these crystallization conditions, the nucleation of ***sod***-$Zn(mIM)_2$ does not favor heterogeneous nucleation around FBSA. Thus, it is apparent that the encapsulation process is mainly based on the adsorption of FBSA on the surfaces of the growing ZIF particles. This is analogous to the encapsulation mechanism previously reported for nanoparticle/***sod***-$Zn(mIM)_2$ composites.[31] Unfortunately, due to the resolution limitation of the CLSM technique, the thickness of the FBSA layer cannot be accurately measured.

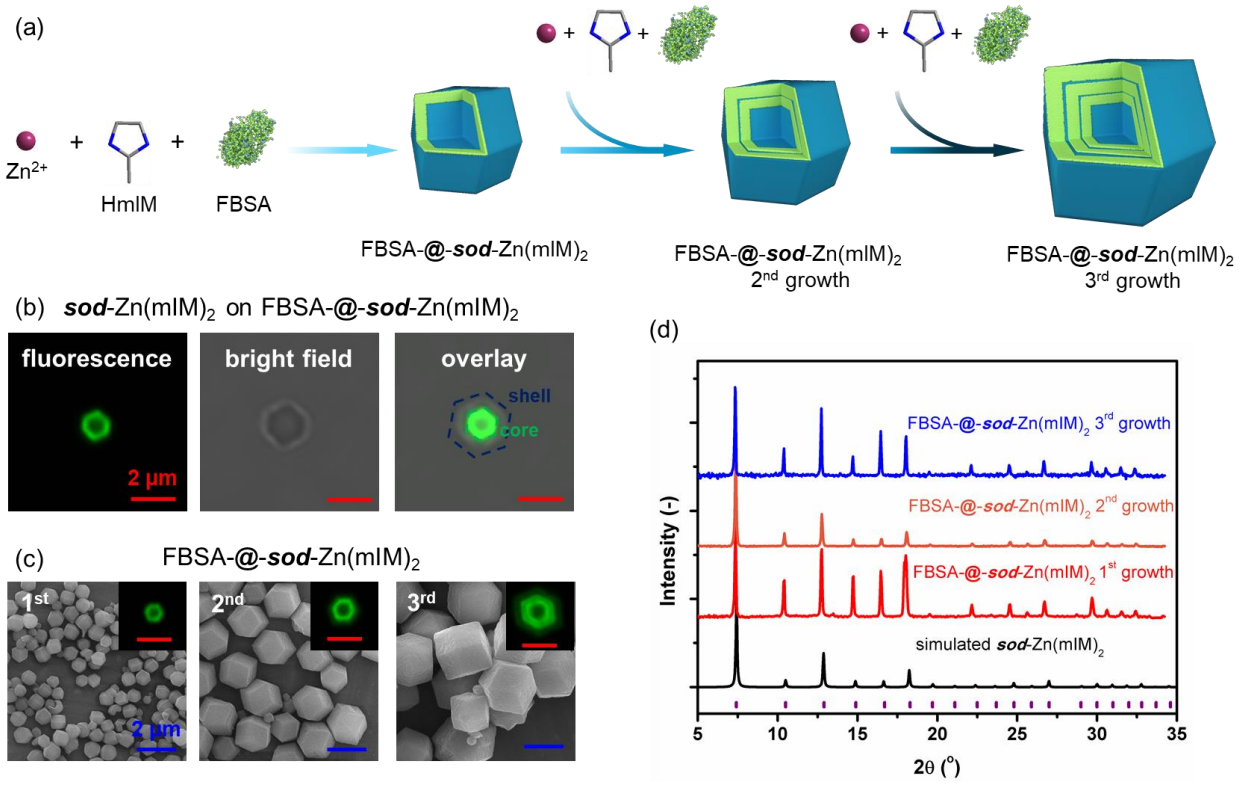

Figure 4. (a) Schematic diagram demonstrating the synthesis method of the multiple-core-shell FBSA-@-***sod***-$Zn(mIM)_2$ composite. (b) Confocal laser scanning micrographs showing the fluorescence, bright field, and overlay images of the ***sod***-$Zn(mIM)_2$ on FBSA-@-***sod***-$Zn(mIM)_2$ core-shell structure. The synthesis method for the ***sod***-$Zn(mIM)_2$ shell is analogous to the FBSA-@-***sod***-$Zn(mIM)_2$ core, however, without the addition of FBSA. (c) SEM images of the multiple-core-shell FBSA-@-***sod***-$Zn(mIM)_2$ composites after first (left), secondary (middle), and tertiary (right) growth. Insects of the SEM images show the fluorescence images of the corresponding FBSA-@-***sod***-$Zn(mIM)_2$ composites. Scale bar in the SEM images (blue) and the fluorescence images (red) represent 2 µm. (d) Simulated PXRD pattern of the ***sod***-$Zn(mIM)_2$ and the FBSA-@-***sod***-$Zn(mIM)_2$ samples after epitaxial growth.

The sub-surface encapsulation of the biomacromolecule in ***sod***-$Zn(mIM)_2$ may pose an additional advantage with respect to mass-diffusion for catalytic application of these materials. On the other hand, the superficial distribution of biomacromolecules in ***sod***-$Zn(mIM)_2$ is likely to reduce the protective capacity offered by the ZIF coating. We suspected that the fluorophore-functionalization would change the surface chemistry of BSA (due to the different structures and functionalities of the fluorophores), and therefore its affinity towards Zn^{2+} ions, thus modify the spatial distribution of the biomolecules within ***sod***-$Zn(mIM)_2$. Besides FITC, rhodamine B isothiocyanate (RbITC) is another widely used fluorescent label to modify proteins and other biomolecules.[35, 36] Compared to fluorescein, rhodamine B contains two diethylamino groups, and this chemical difference between will provide a case for comparison to understand the effect of surface-functionalization of biomolecules on biomimetic mineralization

process. Thus, rhodamine B-tagged BSA (RbBSA) was synthesized and used in the biomineralized growth of RbBSA/***sod***-Zn(mIM)$_2$. In contrast to FBSA-@-***sod***-Zn(mIM)$_2$, CLSM images indicate that the RbBSA molecules are localized in the center and around the surface region of RbBSA/***sod***-Zn(mIM)$_2$ crystallites. We tested the previously developed washing procedure on RbBSA-**on**-***sod***-Zn(mIM)$_2$ crystals to remove the surface-adsorbed RbBSA. However, even at elevated temperature (60 °C) and prolonged treatment time (24 h), the surface-adsorbed RbBSA could not be removed (Figure S23-S23). Thus we could not ascertain whether the fluorescence signal around the RbBSA-@-***sod***-Zn(mIM)$_2$ crystallites originated from surface-adsorbed or superficially localized RbBSA. To gain insight into the surface chemistry of the fluorophore-tagged BSA, we carried out zeta potential analysis for BSA, FBSA, and RbBSA. The zeta potentials of BSA, FBSA, and RbBSA were measured in 640 mM HmIM aqueous solution (adjusted to pH 9.5 by 0.1 M HCl) to simulate the ***sod***-Zn(mIM)$_2$ biocomposites synthesis conditions after mixing of precursors. Interestingly, the zeta potential of BSA was minimally affected by the fluorescein-tag (-9.2 ± 1.1 versus -9.4 ± 1.5 mV). However, rhodamine B decreased the surface potential of BSA to -13.5 ± 0.8 mV. These data indicate that RbBSA will have a stronger affinity for Zn^{2+} ions due to more negative zeta potential, which may explain the centralized location of RbBSA observed in RbBSA-@-***sod***-Zn(mIM)$_2$ as this distribution pattern would be induced by heterogeneous nucleation process.[6, 14] To ascertain the effect of chemical functionalization on protein distribution we examined the CLSM images of biocomposites of fluorescein- and rhodamine B-tagged AOx (F-AOx and Rb-AOx), HRP (F-HRP and Rb-HRP), HGB (F-HGB and Rb-HGB), MB (F-MB and Rb-MB), TR (F-TR and Rb-TR), and urease (F-urease or Rb-urease) (Figure 3 and S24). Similar to BSA, CLSM images indicate that the fluorescein-grafted proteins are predominately localized towards the surface of the ***sod***-Zn(mIM)$_2$ crystals, while the rhodamine B-grafted proteins are centrally localized and surface/sub-surface bound (Figure 3). These data clearly show that the spatial distribution of biomacromolecules within ZIFs crystallites is highly dependent on the surface charge of the protein.

To ensure the complete encapsulation of biomacromoleules, our results suggest that a secondary ZIF shell is necessary. The seed-mediated growth of core-shell structured ZIF crystals is well documented in the literature[37] and we explored this strategy to synthesize a multi-core-shell biomacromolecule-@-***sod***-Zn(mIM)$_2$ composites. In addition to offering enhanced protection, this strategy also opens up the possibility to precisely controlled the spatial localization of multiple biomacromolecules within one ***sod***-Zn(mIM)$_2$ crystal. In a preliminary experiment, a ***sod***-Zn(mIM)$_2$ on FBSA-@-***sod***-Zn(mIM)$_2$ core-shell structure was synthesized by dispersing 10 mg of FBSA-@-***sod***-Zn(mIM)$_2$ in an aqueous solution of HmIM by sonication, followed by the injection of an aqueous solution of Zn(OAc)$_2$ (Figure 4a). The final concentrations for HmIM and Zn(OAc)$_2$ in the reaction mixture were 640 mM and 40 mM, respectively. The reaction mixture was allowed to stand at room temperature for 24 h. PXRD analysis confirmed the phase purity of the sample (Figure S26) and CLSM and SEM images indicated that the synthesis of a core-shell structure was successful (Figure 4b). Comparison of the particle size distribution calculated from SEM images of FBSA-@-***sod***-Zn(mIM)$_2$ and ***sod***-Zn(mIM)$_2$ on FBSA-@-***sod***-Zn(mIM)$_2$, indicate the ***sod***-Zn(mIM)$_2$ shell was approximately 0.55 µm (Figure S27). In the present study, up to three layers of FBSA-@-***sod***-Zn(mIM)$_2$ can be grown within one ***sod***-Zn(mIM)$_2$ crystal (Figure 4c). However, the possibility of forming ***sod***-Zn(mIM)$_2$ crystallite with more than tertiary growth cannot be excluded. As expected, the particle size increase with the introduction of FBSA-@-***sod***-Zn(mIM)$_2$ layers (1.58 ± 0.15, 2.20 ± 0.16, and 2.83 ± 0.24 µm for the first, secondary, and tertiary growth FBSA-@-***sod***-Zn(mIM)$_2$, respectively, Figure 4c). FBSA loadings were calculated to be similar for the first, secondary, and tertiary growth FBSA-@-***sod***-Zn(mIM)$_2$ (0.8 ± 0.1 wt%). To assess the permanent porosity of the core-shell ***sod***-Zn(mIM)$_2$/FBSA biocomposites, 77 K N_2 sorption isotherms were measured (Figure S28). The BET analysis of the data afforded surface area values of 1212.2, 1159.6, and 1072.6 $m^2\ g^{-1}$ for the FBSA-@-***sod***-Zn(mIM)$_2$ samples after first, secondary, and tertiary growth, showing a decrease of porosity relative to pure ***sod***-Zn(mIM)$_2$ (1356.6 $m^2\ g^{-1}$). This is consistent with the presence of non-porous FBSA in the ZIF crystals (Figure 28), additionally this may also be associated with increased defects and the interfaces of the core-shell structures.[6] Importantly, the pore size distribution curves calculated from 77 K N_2 adsorption isotherms demonstrated that the pore structure of the core-shell material is essentially identical to ***sod***-Zn(mIM)$_2$ (Figure S28). The synthesis of biomimetically mineralized core-shell materials offers the potential to: 1) incorporate multiple biomacromolecules within a single crystal in a spatially controlled manner; 2) to introduce different metal ion and/or imidazole ligand within a single biocomposite crystal; 3) control the thickness of each layer by modifying the amount of ***sod***-Zn(mIM)$_2$ precursor in the epitaxial growth reaction.

CONCLUSION

In conclusion, we have established the synthetic conditions required to obtain pure phase biomacromolecule-@-ZIF composites. Accordingly, this work facilitates the design of ZIF-based biocomposites for application to areas such as bio-catalysis, where control of structure properties such as pore size is highly desired. Our data shows that the concentration of the MOF precursors play a dominant role in the resulting ZIF structure topology, with dilute or ligand-deficient ratio yielding less desirable dense phases under biomolecule compatible conditions. In addition, we have ascertained that the surface chemistry of the biomacromolecule appears to influence the spatial location of the protein within the ZIF crystal, thereby providing the opportunity to further tune localisation and properties (i.e. mass transport, improved protection). Reliable enhanced protection and encapsulation was shown to be afforded by seed-mediated growth of core-shell structured ZIF crystals. This present work has significantly advanced

the current understanding of the biomimetic mineralization process and we envisage that it will provide a platform for the future development of these novel systems.

ASSOCIATED CONTENT

Supporting Information. Full analytic details, including XRD patterns, SEM images, CLSM images, FTIR spectra, TGA curves, gas sorption isotherms, and fluorescence spctra. This material is available free of charge via the Internet at http://pubs.acs.org.

AUTHOR INFORMATION

Corresponding Author

*Email: christian.doonan@adelaide.edu.au, paolo.falcaro@tugraz.at.

Author Contributions

All authors have given approval to the final version of the manuscript.

Funding Sources

Australian Research Council Discovery Project (DP170103531).

Notes

The authors declare no competing financial interest.

ACKNOWLEDGMENT

This work was supported by the Australian Research Council under the Discovery Projects Scheme (DP170103531). N. Maddigan acknowledges The University of Adelaide for a Ph.D. Scholarship under the Research Training Program. R. Ricco acknowledges the European Union's Horizon 2020 research and innovation programme under the Marie Skłodowska-Curie grant agreement #748649.The authors acknowledge the facilities, and the scientific and technical assistance of the Australian Microscopy & Microanalysis Research Facility at the Adelaide Microscopy Unit, The University of Adelaide.

REFERENCES

1. Furukawa, H.; Cordova, K. E.; O'Keeffe, M.; Yaghi, O. M., The Chemistry and Applications of Metal-Organic Frameworks. *Science* **2013,** 341, (6149).
2. Kitagawa, S., Porous crystalline materials: closing remarks. *Faraday Discuss.* **2017,** 201, (0), 395-404.
3. Rungtaweevoranit, B.; Diercks, C. S.; Kalmutzki, M. J.; Yaghi, O., Spiers Memorial Lecture: Progress and prospects of reticular chemistry. *Faraday Discuss.* **2017,** 201, (0), 9-45.
4. Guillerm, V.; Kim, D.; Eubank, J. F.; Luebke, R.; Liu, X.; Adil, K.; Lah, M. S.; Eddaoudi, M., A supermolecular building approach for the design and construction of metal-organic frameworks. *Chem. Soc. Rev.* **2014,** 43, (16), 6141-6172.
5. Liang, K.; Coghlan, C. J.; Bell, S. G.; Doonan, C.; Falcaro, P., Enzyme encapsulation in zeolitic imidazolate frameworks: a comparison between controlled co-precipitation and biomimetic mineralisation. *Chem. Commun.* **2016,** 52, (3), 473-476.
6. Liang, K.; Ricco, R.; Doherty, C. M.; Styles, M. J.; Bell, S.; Kirby, N.; Mudie, S.; Haylock, D.; Hill, A. J.; Doonan, C. J.; Falcaro, P., Biomimetic mineralization of metal-organic frameworks as protective coatings for biomacromolecules. *Nat. Commun.* **2015,** 6, 7240.
7. Huo, J.; Aguilera-Sigalat, J.; El-Hankari, S.; Bradshaw, D., Magnetic MOF microreactors for recyclable size-selective biocatalysis. *Chem. Sci.* **2015,** 6, (3), 1938-1943.
8. Li, S.; Dharmarwardana, M.; Welch, R. P.; Ren, Y.; Thompson, C. M.; Smaldone, R. A.; Gassensmith, J. J., Template-Directed Synthesis of Porous and Protective Core–Shell Bionanoparticles. *Angew. Chem., Int. Ed.* **2016,** 55, (36), 10691-10696.
9. Liang, K.; Richardson, J. J.; Cui, J.; Caruso, F.; Doonan, C. J.; Falcaro, P., Metal–Organic Framework Coatings as Cytoprotective Exoskeletons for Living Cells. *Adv. Mater.* **2016,** 28, (36), 7910-7914.
10. Liang, K.; Richardson, J. J.; Doonan, C. J.; Mulet, X.; Ju, Y.; Cui, J.; Caruso, F.; Falcaro, P., An Enzyme-Coated Metal–Organic Framework Shell for Synthetically Adaptive Cell Survival. *Angew. Chem., Int. Ed.* **2017,** 56, (29), 8510-8515.
11. Doonan, C.; Riccò, R.; Liang, K.; Bradshaw, D.; Falcaro, P., Metal–Organic Frameworks at the Biointerface: Synthetic Strategies and Applications. *Acc. Chem. Res.* **2017,** 50, (6), 1423-1432.
12. Park, K. S.; Ni, Z.; Côté, A. P.; Choi, J. Y.; Huang, R.; Uribe-Romo, F. J.; Chae, H. K.; O'Keeffe, M.; Yaghi, O. M., Exceptional chemical and thermal stability of zeolitic imidazolate frameworks. *Proc. Natl. Acad. Sci. U.S.A.* **2006,** 103, (27), 10186-10191.
13. Huang, X.-C.; Lin, Y.-Y.; Zhang, J.-P.; Chen, X.-M., Ligand-Directed Strategy for Zeolite-Type Metal–Organic Frameworks: Zinc(II) Imidazolates with Unusual Zeolitic Topologies. *Angew. Chem., Int. Ed.* **2006,** 45, (10), 1557-1559.
14. Shieh, F.-K.; Wang, S.-C.; Yen, C.-I.; Wu, C.-C.; Dutta, S.; Chou, L.-Y.; Morabito, J. V.; Hu, P.; Hsu, M.-H.; Wu, K. C. W.; Tsung, C.-K., Imparting Functionality to Biocatalysts via Embedding Enzymes into Nanoporous Materials by a de Novo Approach: Size-Selective Sheltering of Catalase in Metal–Organic Framework Microcrystals. *J. Am. Chem. Soc.* **2015,** 137, (13), 4276-4279.
15. Lyu, F.; Zhang, Y.; Zare, R. N.; Ge, J.; Liu, Z., One-Pot Synthesis of Protein-Embedded Metal–Organic Frameworks with Enhanced Biological Activities. *Nano Lett.* **2014,** 14, (10), 5761-5765.
16. Liao, F.-S.; Lo, W.-S.; Hsu, Y.-S.; Wu, C.-C.; Wang, S.-C.; Shieh, F.-K.; Morabito, J. V.; Chou, L.-Y.; Wu, K. C. W.; Tsung, C.-K., Shielding against Unfolding by Embedding Enzymes in Metal–Organic Frameworks via a de Novo Approach. *J. Am. Chem. Soc.* **2017,** 139, (19), 6530-6533.
17. Zhang, J.-P.; Zhang, Y.-B.; Lin, J.-B.; Chen, X.-M., Metal Azolate Frameworks: From Crystal Engineering to Functional Materials. *Chem. Rev.* **2012,** 112, (2), 1001-1033.
18. Hayashi, H.; Cote, A. P.; Furukawa, H.; O/'Keeffe, M.; Yaghi, O. M., Zeolite A imidazolate frameworks. *Nat. Mater.* **2007,** 6, (7), 501-506.
19. Pan, Y.; Liu, Y.; Zeng, G.; Zhao, L.; Lai, Z., Rapid synthesis of zeolitic imidazolate framework-8 (ZIF-8) nanocrystals in an aqueous system. *Chem. Commun.* **2011,** 47, (7), 2071-2073.
20. Bommarius, A. S.; Paye, M. F., Stabilizing biocatalysts. *Chem. Soc. Rev.* **2013,** 42, (15), 6534-6565.
21. Bornscheuer, U. T.; Huisman, G. W.; Kazlauskas, R. J.; Lutz, S.; Moore, J. C.; Robins, K., Engineering the third wave of biocatalysis. *Nature* **2012,** 485, (7397), 185-194.
22. Shi, Q.; Chen, Z.; Song, Z.; Li, J.; Dong, J., Synthesis of ZIF-8 and ZIF-67 by Steam-Assisted Conversion and an Investigation of Their Tribological Behaviors. *Angew. Chem., Int. Ed.* **2011,** 50, (3), 672-675.

23. Katsenis, A. D.; Puškarić, A.; Štrukil, V.; Mottillo, C.; Julien, P. A.; Užarević, K.; Pham, M.-H.; Do, T.-O.; Kimber, S. A. J.; Lazić, P.; Magdysyuk, O.; Dinnebier, R. E.; Halasz, I.; Friščić, T., In situ X-ray diffraction monitoring of a mechanochemical reaction reveals a unique topology metal-organic framework. *Nat. Commun.* **2015,** 6, 6662.

24. Akimbekov, Z.; Katsenis, A. D.; Nagabhushana, G. P.; Ayoub, G.; Arhangelskis, M.; Morris, A. J.; Friščić, T.; Navrotsky, A., Experimental and Theoretical Evaluation of the Stability of True MOF Polymorphs Explains Their Mechanochemical Interconversions. *J. Am. Chem. Soc.* **2017,** 139, (23), 7952-7957.

25. Baburin, I. A.; Leoni, S., The energy landscapes of zeolitic imidazolate frameworks (ZIFs): towards quantifying the presence of substituents on the imidazole ring. *J. Mater. Chem.* **2012,** 22, (20), 10152-10154.

26. Baburin, I. A.; Leoni, S., Modelling polymorphs of metal-organic frameworks: a systematic study of diamondoid zinc imidazolates. *CrystEngComm* **2010,** 12, (10), 2809-2816.

27. Cui, J.; Feng, Y.; Lin, T.; Tan, Z.; Zhong, C.; Jia, S., Mesoporous Metal–Organic Framework with Well-Defined Cruciate Flower-Like Morphology for Enzyme Immobilization. *ACS Appl. Mater. Interfaces* **2017,** 9, (12), 10587-10594.

28. Jian, M.; Liu, B.; Liu, R.; Qu, J.; Wang, H.; Zhang, X., Water-based synthesis of zeolitic imidazolate framework-8 with high morphology level at room temperature. *RSC Adv.* **2015,** 5, (60), 48433-48441.

29. Li, P.; Modica, J. A.; Howarth, A. J.; Vargas L., E.; Moghadam, P. Z.; Snurr, R. Q.; Mrksich, M.; Hupp, J. T.; Farha, O. K., Toward Design Rules for Enzyme Immobilization in Hierarchical Mesoporous Metal-Organic Frameworks. *Chem* **2016,** 1, (1), 154-169.

30. Ma, L.; Falkowski, J. M.; Abney, C.; Lin, W., A series of isoreticular chiral metal–organic frameworks as a tunable platform for asymmetric catalysis. *Nat. Chem.* **2010,** 2, (10), 838-846.

31. Lu, G.; Li, S.; Guo, Z.; Farha, O. K.; Hauser, B. G.; Qi, X.; Wang, Y.; Wang, X.; Han, S.; Liu, X.; DuChene, J. S.; Zhang, H.; Zhang, Q.; Chen, X.; Ma, J.; Loo, S. C. J.; Wei, W. D.; Yang, Y.; Hupp, J. T.; Huo, F., Imparting functionality to a metal–organic framework material by controlled nanoparticle encapsulation. *Nat. Chem.* **2012,** 4, (4), 310-316.

32. Phan, A.; Doonan, C. J.; Uribe-Romo, F. J.; Knobler, C. B.; O'Keeffe, M.; Yaghi, O. M., Synthesis, Structure, and Carbon Dioxide Capture Properties of Zeolitic Imidazolate Frameworks. *Acc. Chem. Res.* **2010,** 43, (1), 58-67.

33. Yang, J.; Zhang, Y.-B.; Liu, Q.; Trickett, C. A.; Gutiérrez-Puebla, E.; Monge, M. Á.; Cong, H.; Aldossary, A.; Deng, H.; Yaghi, O. M., Principles of Designing Extra-Large Pore Openings and Cages in Zeolitic Imidazolate Frameworks. *J. Am. Chem. Soc.* **2017,** 139, (18), 6448-6455.

34. Nordin, N. A. H. M.; Ismail, A. F.; Mustafa, A.; Goh, P. S.; Rana, D.; Matsuura, T., Aqueous room temperature synthesis of zeolitic imidazole framework 8 (ZIF-8) with various concentrations of triethylamine. *RSC Adv.* **2014,** 4, (63), 33292-33300.

35. Wu, X.; Ge, J.; Yang, C.; Hou, M.; Liu, Z., Facile synthesis of multiple enzyme-containing metal-organic frameworks in a biomolecule-friendly environment. *Chem. Commun.* **2015,** 51, (69), 13408-13411.

36. Michael Mullins, J., Overview of Fluorophores. In *Immunocytochemical Methods and Protocols*, Javois, L. C., Ed. Humana Press: Totowa, NJ, 1995; pp 107-116.

37. Tang, J.; Salunkhe, R. R.; Liu, J.; Torad, N. L.; Imura, M.; Furukawa, S.; Yamauchi, Y., Thermal Conversion of Core–Shell Metal–Organic Frameworks: A New Method for Selectively Functionalized Nanoporous Hybrid Carbon. *J. Am. Chem. Soc.* **2015,** 137, (4), 1572-1580.